Comparison of Reduced Order Spacecraft Charging Models for Electrostatic Proximity Operations

Julian Hammerl
Graduate Research Assistant
Aerospace Engineering Sciences
University of Colorado Boulder
Boulder, Colorado 80303
julian.hammerl@colorado.edu

Kaylee Champion
Graduate Research Assistant
Aerospace Engineering Sciences
University of Colorado Boulder
Boulder, Colorado 80303

Hanspeter Schaub
Professor and Department Chair
Schaden Leadership Chair
Aerospace Engineering Sciences
University of Colorado Boulder
Boulder, Colorado 80303

***Abstract*—Spacecraft charge in orbit due to naturally occurring electric currents from the ambient plasma and the Sun, and artificial currents produced by devices such as an electron gun. This results in electrostatic forces and torques between two spacecraft in close proximity that can perturb the relative motion during on-orbit servicing, assembly and manufacturing (OSAM) operations, or be utilized to remove or detumble dysfunctional satellites. In prior work on electrostatic proximity operations, typically charging models based on spherical current collection were used to compute the electrostatic potential, and that potential was prescribed to be constant in relative motion simulations. In this work, several spacecraft charging models are compared, including a simple sphere model, an adjusted sphere model, and a faceted model. The faceted model is promising because its total surface area is more accurate, and it allows for the consideration of a time-varying sunlit area. Using the faceted model, it is shown that the orientation of the spacecraft with respect to the sun can significantly affect the equilibrium potential and the resulting force and torque. This is demonstrated by a charged attitude motion simulation for the Electrostatic Tractor debris removal concept.**

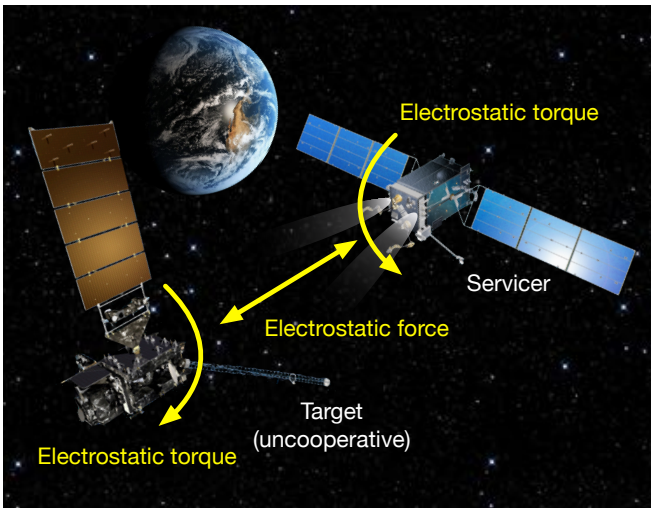

Figure 1. Concept Figure of electrostatic forces and torques

1. INTRODUCTION

Spacecraft naturally build up electric potentials in orbit due to several electric currents in the space environment, such as the photoelectric current from the Sun or the electron and ion current from the ambient plasma [1, Chapter 1]. Spacecraft charging is usually not a concern in Low Earth Orbit (LEO) due to the dense and low-energy plasma, with the exception of a few distinct scenarios such as when a spacecraft is located at auroral latitudes during auroral activities. In high earth orbit, such as the Geostationary Earth Orbit (GEO) or cislunar space the plasma is tenuous and energetic, resulting in high electric potentials reaching tens of kilovolts in eclipse. Record charging events of up to -19 kV were experienced by the Applied Technology Satellite 6 (ATS-6) in GEO [2].

Spacecraft charging affects spaceflight in various ways. Even though modern spacecraft design guidelines recommend to connect all components to one common ground such that all components charge to the same potential [3, Chapter 3], this is not always possible and often not the case for old or retired satellites. Arcing can occur between two components of a satellite if they are charged to different potentials, which potentially reduces the lifetime of solar panels, for example [4], [5]. Electrostatic discharges can occur between two charged spacecraft during docking if the difference in electric potentials is large. One consequence of spacecraft charging that has received increased attention over the last decade are the electrostatic forces that act on two charged spacecraft in close proximity operations (Fig. 1). Electrostatic perturbations can significantly influence On-Orbit Servicing, Assembly and Manufacturing (OSAM) operations [6]. When an uncooperative target satellite is approached by a servicing satellite, the target starts to tumble due to the electrostatic torques if its center of mass is not aligned with its center of charge. The servicer needs to match this rotation to maintain a constant relative orientation with the target during rendezvous and docking. This increases fuel consumption and complicates servicing operations. The electrostatic forces and torques can also be utilized to remove space debris from geostationary orbit with the Electrostatic Tractor (ET) active debris removal method [7], or to detumble uncooperative spacecraft [8].

Prior work on the effects of electrostatic perturbations on proximity operations investigated adjusted approach trajectories that minimize the electrostatic torques and the resulting rotational rate of the target satellite. A relative motion controller that feeds forward on the expected electrostatic perturbations to improve rendezvous performance was also studied [9]. However, all prior work prescribed electric potentials of 10 kV for each spacecraft assuming extreme charging scenarios, without considering the interactions of the spacecraft with the plasma environment. Time varying potentials about the nominal potential of 10 kV were taken into account by introducing random variation, but this does not accurately represent the changing space environment around the Earth

978-1-6654-9032-0/23/$31.00 ©2023 IEEE

or Moon. Spacecraft charging analysis has been done for the Electrostatic Tractor [10], [11]. The effect of the debris attitude on the electrostatic force and consequently the reorbit performance has also been investigated [12]. However, the effect of the debris attitude on the electric potential, which also affects the electrostatic force, has been neglected.

In this work, the natural electric potentials experienced by a spacecraft in GEO and cislunar space are studied. To determine the equilibrium potential of complex-shaped satellites for science purposes or mission planning, numerical tools such as NASCAP-2k or SPIS are frequently used. However, these software frameworks require several minutes to compute the electric potential, making them unsuited for dynamic simulations over an entire orbit. Instead, the following three analytical spacecraft charging models are used to compare their accuracy with a truth model from NASCAP-2k. The first model assumes a spherical spacecraft, the second employs an adjusted sphere model that is tuned for a specific spacecraft using NASCAP-2k, and the third model divides the spacecraft into several facets while neglecting self-shadowing. With these models, the natural potentials in orbit around the Earth or Moon can be efficiently approximated and the resulting electrostatic forces and torques are computed using the Multi-Sphere Method [13]. Additionally, the faceted model allows for the consideration of time-varying potentials due to the rotation of the debris and its effect on the Electrostatic Tractor reorbit process.

2. BACKGROUND

Various electric currents in the space environment cause spacecraft to charge in orbit. The plasma in space contains charged particles such as electrons and ions that transfer their charge to the spacecraft if they impact it [1, Chapter 1]. The resulting currents are referred to as the electron and ion plasma currents, respectively. As electrons and ions penetrate into the surface material of the spacecraft, they transfer some of their energy to nearby electrons in the material. If enough energy is transferred, one or more secondary electrons leave the surface material with low kinetic energies of a few electron-volts (eV), resulting in the so-called secondary electron (SE) current [1, Chapter 3]. An incident electron can also be backscattered. In this case, an electron enters and leaves the surface material, resulting in the backscattered electron current [1, Chapter 3]. A spacecraft in sunlight is also subject to the photoelectric current. The incoming electromagnetic radiation from the Sun excites electrons in the surface material of the spacecraft that, similar to the secondary electrons, leave the material with low energy [1, Chapter 7].

Spacecraft Charging Model

The electron I_e and ion I_i plasma currents are modeled using a particle flux $F(E)$ of the electrons or ions distributed over particle energy E (measured in eV) [14], [15], [11]

$$I_{e/i}(\phi) = qA \int_L^\infty \left(\frac{E}{E \pm \phi} \right) F_{e/i}(E \pm \phi) \, \mathrm{dE} \qquad (1)$$

with the electric potential of the spacecraft ϕ, particle charge q and surface area of the spacecraft A that is exposed to the plasma. Index e denotes electrons and index i denotes ions. The lower bound L of the integral is 0 for the repelled particles (e.g. for electrons if $\phi < 0$) and $|\phi|$ for the attracted particles. The upper sign of $\pm$ applies to ions and the lower sign to electrons, while ϕ may be positive or negative. The ambient electron flux $F_e(E)$ is used for the plasma electron current and the ambient ion flux $F_i(E)$ is used for the plasma ion current.

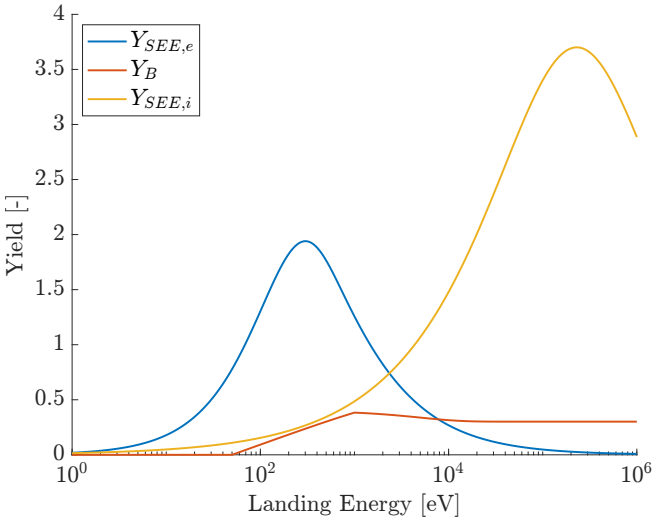

Figure 2. Secondary electron yield (induced by electrons and ions) and backscattered electron yield

If the plasma is Maxwellian, the flux distribution can be described using the plasma temperature T (measured in eV) and plasma density n [14]

$$F(E) = \sqrt{\frac{q_0}{2\pi T m}} \frac{E}{T} n \exp\left(-\frac{E}{T}\right) \qquad (2)$$

and the plasma currents for a spherical spacecraft simplify to [16, Chapter 4]

$$I_e(\phi) = \begin{cases} -\dfrac{A q_0 n_e w_e}{4} e^{\phi/T_e} & \text{if} \quad \phi \leq 0 \\ -\dfrac{A q_0 n_e w_e}{4} \left(1 + \frac{\phi}{T_e}\right) & \text{if} \quad \phi > 0 \end{cases} \qquad (3)$$

for the electron current and

$$I_i(\phi) = \begin{cases} \dfrac{A q_0 n_i w_i}{4} \left(1 - \frac{\phi}{T_i}\right) & \text{if} \quad \phi \leq 0 \\ \dfrac{A q_0 n_i w_i}{4} e^{-\phi/T_i} & \text{if} \quad \phi > 0 \end{cases} \qquad (4)$$

for the ion current, where the unsigned elementary charge q_0 in Coulombs is used. The average thermal velocity is $w = \sqrt{8 T_{e/i} / (m_{e/p} \pi)}$, using the mass of an electron m_e for the electron current and the mass of a proton m_p for the ion current (assuming that the plasma consists solely of protons).

The secondary electron and backscattered currents are modeled as

$$I_{SEE/B}(\phi) = q_0 A \int_L^\infty Y(E) \left(\frac{E}{E \pm \phi} \right) F(E \pm \phi) \, \mathrm{dE} \qquad (5)$$

where $Y(E)$ serves as a placeholder for the electron yield, i.e. the average number of secondary electrons (or backscattered electrons) released per incident electron with landing energy

E, see Fig. 2. The secondary electron yield due to incoming electrons is computed by [14]

$$Y_{ee}(E,\psi) = c_1 \int_0^R \left|\frac{\mathrm{dE}}{\mathrm{dx}}\right| \mathrm{e}^{-\mathrm{c_2 x}\cos\psi}\,\mathrm{dx} \tag{6}$$

where x is the path length of the incident electron, R is the maximum penetration length (range) and ψ is the angle of incidence of the incident electron. The stopping power is [14]

$$\frac{\mathrm{dE}}{\mathrm{dx}} = \left(\frac{\mathrm{dR}}{\mathrm{dE}}\right)^{-1} + \left(\frac{\mathrm{d^2R}}{\mathrm{dE^2}}\right)\left(\frac{\mathrm{dR}}{\mathrm{dE}}\right)^{-3} x \tag{7}$$

and the range is equal to

$$R = b_1 E^{q_1} + b_2 E^{q_2} \tag{8}$$

with material parameters b_1, b_2, q_1, q_2. For aluminum, the values $b_1 = 154$ Å, $b_2 = 220$ Å, $q_1 = 0.8$ and $q_2 = 1.76$ are used, assuming that the landing energy is provided in keV for this equation. The constants c_1 and c_2 are fitted numerically to obtain a yield curve for normal incidence ($\psi = 0$) that has the maximum yield $Y_{\max}$ at an energy $E_{\max}$. For aluminum, $Y_{\max} = 0.97$ and $E_{\max} = 0.3$ keV are used, yielding $c_1 = 8.5467$ and $c_2 = 0.0276$. Finally, the yield for isotropic flux is about two times the yield for normal incidence [14], which gives us the secondary electron yield due to electron impact used in this work:

$$Y_{SEE,e}(E) = 2Y_{ee}(E,0) \tag{9}$$

The backscattered electron yield is based on the albedo for normal incidence A_0 and isotropic flux A_I

$$A_0 = 1 - \left(\frac{2}{e}\right)^a \tag{10}$$

$$A_I = 2\frac{1 - A_0(1 - \log A_0)}{(\log A_0)^2} \tag{11}$$

with $a = 0.0375Z$ and atomic number Z, which is then multiplied by several heaviside step functions to account for special low energy cases [14]

$$Y_B(E) = \left(\frac{H(1-E)H(E-0.05)\log(E/0.05)}{\log 20} + H(E-1)\right)\cdot\left(\frac{\exp(-E/5)}{10} + A_{0/I}\right) \tag{12}$$

In the equation above, E is the energy of the incident electron in keV, $H(x)$ is the heaviside step function, $\log$ is the logarithm with base 10, and either A_0 or A_I is substituted for $A_{0/I}$ depending on the type of flux. The atomic number of $Z = 13$ is used for aluminum, and isotropic flux is assumed. The factor of two for the isotropic flux yield is already considered in the albedo.

Secondary electrons can also be excited by incoming ions. The corresponding yield is modeled by [14]

$$Y_{SEE,i}(E) = 2\frac{\beta E^{1/2}}{1 + E/E_{max,i}} \tag{13}$$

where E is the energy of the incident ion in keV, $E_{max,i}$ is the energy of the maximum yield, and β is a scaling parameter. For aluminum, $E_{\max,i} = 230$ keV and β = 0.244. The factor of 2 accounts for the isotropic flux. Given the energy dependent yield from Eqs. (9), (12) and (13), one computes the secondary electron current due to electrons $I_{SEE,e}$ and backscattered electron current I_B using the ambient electron flux $F_e(E)$ and secondary electron current due to ions $I_{SEE,i}$ using the ambient ion flux $F_i(E)$ with Eq. (5). More illustratively, given the mean yield over all energies (e.g. for secondary electron emission due to electron impact)

$$< Y_{SEE,e} >= \frac{\int_L^\infty Y(E)\big(E/(E\pm\phi)\big)F(E\pm\phi)\mathrm{dE}}{\int_L^\infty \big(E/(E\pm\phi)\big)F(E\pm\phi)\mathrm{dE}} \tag{14}$$

one can calculate the secondary current by

$$I_{SEE,e}(\phi) =< Y_{SEE,e} > \cdot I_e(\phi) \tag{15}$$

Note that the secondary electrons are emitted with very low energy. If the spacecraft is charged negatively, these electrons are accelerated away from the spacecraft. In the case of a positively charged spacecraft, the secondary electrons are attracted back to the spacecraft, as they do not have enough energy to escape. Thus, for a positively charged spacecraft, the secondary electron currents are negligible.

The photoelectric current is equal to [1, Chapter 7]

$$I_{ph}(\phi) = \begin{cases} j_{ph,0}A_{ph} & \text{if} \quad \phi \le 0 \\ j_{ph,0}A_{ph}e^{-\phi/T_{ph}} & \text{if} \quad \phi > 0 \end{cases} \tag{16}$$

where $j_{ph,0}$ and T_{ph} are the flux and temperature of the emitted photoelectrons, and A_{ph} is the projected area of the spacecraft that faces the sun. Values of $j_{ph,0} = 20$ μA/m^2 and $T_{ph} = 2$ eV are used in this work [10]. Similar to secondary electrons, photoelectrons are emitted with very low energy, so for a positively charged spacecraft the photoelectric current drops off exponentially.

The currents discussed so far occur naturally in space. One artificial type of current is electron beam emission and impact. Consider an electron gun attached to a servicing satellite and aimed at a target object, as proposed for the Electrostatic Tractor active debris removal method [7]. The current due to the electron gun on the servicer is equal to [10]

$$I_{EB,S}(\phi_T,\phi_S) = \begin{cases} I_{EB} & \text{if} \quad E_{EB} > \phi_S - \phi_T \\ 0 & \text{if} \quad E_{EB} \le \phi_S - \phi_T \end{cases} \tag{17}$$

where I_{EB} and E_{EB} are the operating current and energy of the electron gun, and ϕ_S and ϕ_T are the electric potentials of the servicer and the target, respectively. Because the initial kinetic energy of the electron beam electrons is equal to E_{EB}, the beam only reaches the target if the initial beam energy E_{EB} is greater than the electric potential difference $\phi_S - \phi_T$ between the two spacecraft. Otherwise, the beam electrons are attracted back to the servicer and the net current is equal to zero. For the servicing satellite, the beam current is positive due to the emission of electrons. For the target satellite, the electron beam current is equal to [10]

$$I_{EB,T}(\phi_T,\phi_S) = \begin{cases} -\alpha_{EB}I_{EB} & \text{if} \quad E_{EB} > \phi_S - \phi_T \\ 0 & \text{if} \quad E_{EB} \le \phi_S - \phi_T \end{cases} \tag{18}$$

Due to the expansion and deflection of the beam [17], only a fraction α_{EB} of the beam hits the target. For simplicity, $\alpha_{EB} = 1$ is assumed in this work. The electron beam

also excites secondary $I_{SEE,EB}(\phi_T, \phi_S)$ and backscattered electron emission $I_{B,EB}(\phi_T, \phi_S)$ from the target, computed by

$$I_{SEE/B,EB}(\phi_T, \phi_S) = Y_{SEE,e/B}(E_{\text{eff}}) \cdot I_{EB,T}(\phi_T, \phi_S) \tag{19}$$

where $E_{\text{eff}} = E_{EB} - \phi_S + \phi_T$ is the landing energy of the electron beam.

If the sum of all currents is equal to zero, the electric potential is at equilibrium. Thus, the equilibrium potential is found by finding the root of the equation

$$\begin{aligned} I_{\text{tot},S}(\phi_T, \phi_S) = I_e(\phi_S) + I_i(\phi_S) + I_{SEE,e}(\phi_S) + I_B(\phi_S) \\ + I_{SEE,i}(\phi_S) + I_{ph}(\phi_S) + I_{EB,S}(\phi_T, \phi_S) \end{aligned} \tag{20}$$

for the servicing satellite and

$$\begin{aligned} I_{\text{tot},T}(\phi_T, \phi_S) = I_e(\phi_T) + I_i(\phi_T) + I_{SEE,e}(\phi_T) + I_B(\phi_T) \\ + I_{SEE,i}(\phi_T) + I_{ph}(\phi_T) + I_{EB,T}(\phi_T, \phi_S) \\ + I_{SEE,EB}(\phi_T, \phi_S) + I_{B,EB}(\phi_T, \phi_S) \end{aligned} \tag{21}$$

for the target spacecraft.

Note that, even though the equilibrium potential of the servicer and target are computed independently in this work, the charging behavior of the two spacecraft is coupled. A highly charged spacecraft might cause changes in the ambient plasma, which affects the potential of a nearby craft. Additionally, a positively charged servicer might attract secondary and photoelectrons generated from a less positively charged target, resulting in a target spacecraft that is charged more positively than one would expect according to the isolated charging model used in this work. The consideration of such coupled effects is left for future work.

Multi-Sphere Method

The Multi-Sphere Method (MSM) uses several spheres to approximate the charge distribution of complex shapes and is implemented here to calculate the electrostatic force and torque acting on each spacecraft [13], [18]. The voltage to charge relation is given by

$$\begin{bmatrix} V_1 \\ V_2 \\ \vdots \\ V_n \end{bmatrix} = k_c \begin{bmatrix} 1/R_1 & 1/r_{1,2} & \cdots & 1/r_{1,n} \\ 1/r_{2,1} & 1/R_2 & \cdots & 1/r_{2,n} \\ \vdots & \vdots & \ddots & \vdots \\ 1/r_{n,1} & 1/r_{n,2} & \cdots & 1/R_n \end{bmatrix} \begin{bmatrix} Q_1 \\ Q_2 \\ \vdots \\ Q_n \end{bmatrix} \tag{22}$$

where V_i, Q_i, R_i are the electric potential, electric charge and radius of the i-th sphere, respectively, $r_{i,j}$ is the distance between the i-th and j-th sphere, and k_c is the Coulomb constant. Knowing the charge on each sphere, the electrostatic force acting on spacecraft 1 is computed by

$$\boldsymbol{F}_1 = -k_c \sum_{j=1}^{n_1} \boldsymbol{Q}_{1_j} \left(\sum_{i=1}^{n_2} \frac{\boldsymbol{Q}_{2_i}}{r_{i,j}^3} \boldsymbol{r}_{i,j} \right) \tag{23}$$

and the electrostatic torque acting on spacecraft 1 about point 0 is computed by

$$\boldsymbol{L}_{1,0} = -k_c \sum_{j=1}^{n_1} \boldsymbol{r}_j \times \boldsymbol{Q}_{1_j} \left(\sum_{i=1}^{n_2} \frac{\boldsymbol{Q}_{2_i}}{r_{i,j}^3} \boldsymbol{r}_{i,j} \right) \tag{24}$$

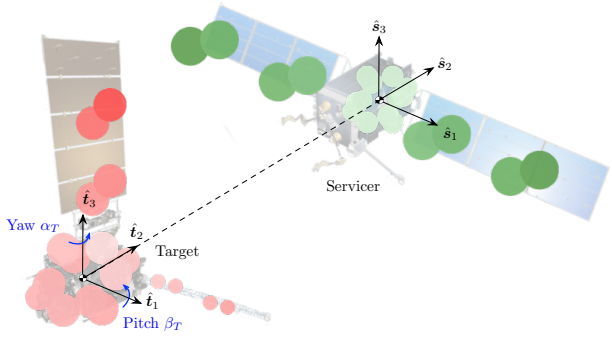

Figure 3. Multi-Sphere Spacecraft Models. Target spacecraft on the left, servicing spacecraft on the right

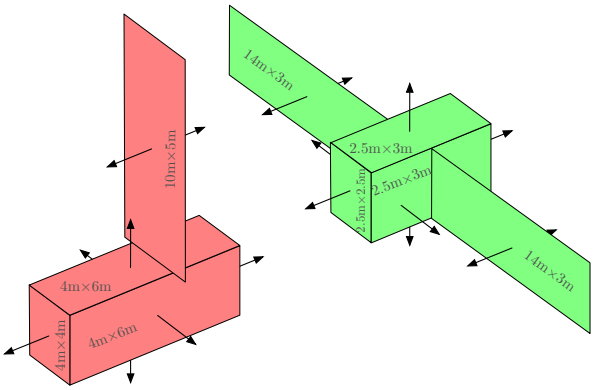

Figure 4. Faceted Spacecraft Model

In the equations above, $\boldsymbol{Q}_1$ includes the charges of the n_1 spheres of spacecraft 1, $\boldsymbol{Q}_2$ includes the charges of the n_2 spheres of spacecraft 2, and $\boldsymbol{r}_j$ is the vector from the point 0 to the j-th sphere. The Multi-Sphere models used in this work are shown in Fig. 3. The target is based on the GOES-R satellite and is interesting due to its asymmetric shape, while the servicer is based on an SSL-1300 satellite bus. Previous work shows that a model with 20 spheres per spacecraft, distributed on the surface, provides a good representation of the electrostatic forces while requiring about 1/6 of the computational effort than a model with 80 spheres per spacecraft [19]. Figure 3 also shows the body frame of the target $\mathcal{T}$: $\{\hat{\boldsymbol{t}}_1, \hat{\boldsymbol{t}}_2, \hat{\boldsymbol{t}}_3\}$ and the servicer $\mathcal{S}$: $\{\hat{\boldsymbol{s}}_1, \hat{\boldsymbol{s}}_2, \hat{\boldsymbol{s}}_3\}$ in their nominal orientation. A 3-2-1 Euler rotation sequence with yaw angle α_T and pitch angle β_T is used to describe the orientation of the target. A rotation about the $\hat{\boldsymbol{t}}_2$ axis is assumed not to provide any additional insight, so the rotation about this axis is always set to zero to improve the visualization of the results by using only two rotation angles. The reference orientation for any rotations is the nominal orientation shown in the figure, where the both body frames are aligned with the Hill frame.

Faceted Model

A faceted model is implemented to compute the projected sunlit area of the spacecraft that is facing the sun, neglecting

self-shadowing. The spacecraft is divided into n facets with area A_i and normal vector $\hat{\boldsymbol{n}}_i$ of the i-th facet. The projected sunlit area of the i-th facet is equal to

$$A_{ph,i} = \begin{cases} A_i \cos\theta_{s,i} = A_i \frac{\hat{\boldsymbol{s}}\cdot\hat{\boldsymbol{n}}_i}{|\hat{\boldsymbol{s}}|\cdot|\hat{\boldsymbol{n}}_i|} & \text{if} \quad \hat{\boldsymbol{s}}\cdot\hat{\boldsymbol{n}}_i > 0 \\ 0 & \text{if} \quad \hat{\boldsymbol{s}}\cdot\hat{\boldsymbol{n}}_i \leq 0 \end{cases} \tag{25}$$

where $\theta_{s,i}$ is the angle between the sun direction $\hat{\boldsymbol{s}}$ and the normal to the surface $\hat{\boldsymbol{n}}_i$. If the dot product $\hat{\boldsymbol{s}}\cdot\hat{\boldsymbol{n}}_i$ is negative, the area is facing away from the sun so the sunlit area for that facet is set equal to 0. The total projected area of the spacecraft that is facing the sun is then

$$A_{ph} = \sum_{i=1}^{n} A_{ph,i} \tag{26}$$

Figure 4 shows the faceted models for the GOES-R and SSL-1300 spacecraft, including the dimensions and normal vectors or the facets.

Rotational Dynamics

The rotational dynamics of the target are given by [20, Chapter 4]

$$[I_T]\dot{\boldsymbol{\omega}} = -[\tilde{\boldsymbol{\omega}}][I_T]\boldsymbol{\omega} + \boldsymbol{L}_c \tag{27}$$

where $[I_T]$ is the inertia matrix of the target, $\boldsymbol{\omega}$ is the angular velocity of the target, and $\boldsymbol{L}_c$ is the electrostatic torque acting on the target. The skew-symmetric matrix $[\tilde{\boldsymbol{\omega}}]$ is used as the cross-product equivalent matrix operator of $\boldsymbol{\omega}$. The inertia matrix is obtained from a CAD model of the target that is generated using publicly available size and mass information of a GOES-R satellite [21]. The attitude of the servicer is held constant at the desired orientation, so no rotational dynamics need to be implemented for the servicer.

3. Comparison with Nascap-2k

To verify the accuracy of the implemented charging model, simulations are performed with the Nascap-2k spacecraft charging software for several spacecraft shapes, using the *Analytic Currents*, *Surface Charging* mode in Nascap. The shapes in this study include a sphere with a radius of 1 m, the GOES-R and the SSL-1300 spacecraft. A severe charging environment is chosen based on the GEO worst-case scenario in Nascap, with $n_e = 1.12 \cdot 10^6$ m^{-3}, $T_e = 12{,}000$ eV, $n_i = 2.36 \cdot 10^5$ m^{-3} and $T_i = 29{,}500$ eV, with the spacecraft in eclipse and no active electron beam. Figure 5 shows the absolute difference between the currents obtained in Nascap and those computed with the implemented charging model as a function of the spacecraft potential, where the different line types indicate the shape model, and the line color specifies the currents.

The electron I_e and ion I_i plasma currents agree reasonably well with errors less than 1 µA across all shapes and potentials. This is important as the secondary and backscattered currents depend on the plasma currents. The random behavior that is visible for the plasma currents is due to the fact that the currents from Nascap-2k are only computed with four significant digits, while a higher precision is used in Matlab. Large differences exceeding 1 µA are observed for the secondary electron current due to electron impact $I_{SEE,e}$ and the backscattered electron current I_B, especially for the non-spherical shapes. Interestingly, the figure shows a linear trend between the errors of these two currents and the spacecraft potential. Given the logarithmic scale of the

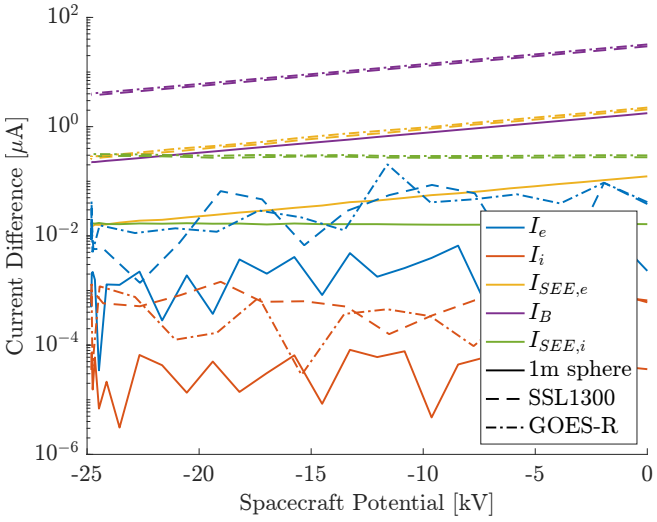

Figure 5. Comparison with Nascap-2k

plot, this is actually an exponential trend. This trend is expected, because the currents $I_{SEE,e}$ and I_B are related to the electron plasma current I_e, which decreases exponentially in magnitude with increasing negative potential, see Eq. (3). That is, the variation of the difference in $I_{SEE,e}$ and I_B with the potential is due to the changing magnitude of I_e, while the underlying error in the secondary and backscattered electron yield is nearly constant across all potentials. The deviation of the secondary electron current due to ion impact $I_{SEE,i}$ is smaller and does not show a clear trend with the spacecraft potential. Again, the errors for the spherical shaped spacecraft are smaller. All of the currents shown in Fig. 5 are directly affected by the ambient plasma currents, which are scaled by the total spacecraft surface area that is exposed to the plasma. For the 1 m sphere, the surface area is about 12.6 m^2, while it is 228 m^2 for the GOES-R and 210.5 m^2 for the SSL-1300 satellite. Due to the larger surface area, the current difference is higher for the GOES-R and SSL-1300 shapes, while the difference in flux is similar.

Table 1 displays the equilibrium potential for the given charging environment, and the various currents for a potential of -24.810 kV (corresponding to the equilibrium potential obtained in Nascap). The difference between the equilibrium potential computed with Nascap and the implemented charging model is about 3%, while the difference for most currents is in the order of 1% or lower. Only the backscattered electron current deviates significantly with an error of 12%.

4. Faceted Model Analysis

The photoelectric effect provides a strong, naturally occurring current in the space environment that is scaled by the sunlit area of the spacecraft. If a spherical shape is used for the charging model, the sunlit area is independent of the orientation. However, for more complex shapes such as satellites, the sunlit area can vary significantly. The faceted model described earlier is implemented to account for these variations. The plasma parameters used here correspond to a local time of $LT = 12$ h in geostationary orbit and a planetary K-index of $K_p = 2$ according to Ref. [22], and are equal to $n_e = 6 \cdot 10^5$ m^{-3}, $T_e = 700$ eV, $n_i = 6.5 \cdot 10^5$ m^{-3}

	Eq. Pot. [kV]	I_e [µA]	I_i [µA]	$I_{SEE,e}$ [µA]	I_B [µA]	$I_{SEE,i}$ [µA]
Nascap	-24.810	-5.229	0.587	1.068	1.842	1.732
Model	-25.560	-5.228	0.587	1.083	1.619	1.748
Difference	3 %	-0.014 %	0.006 %	1.5 %	-12 %	0.97 %

Table 1. Comparison between Nascap-2k and implemented charging model for 1 m radius sphere at Nascap equilibrium potential

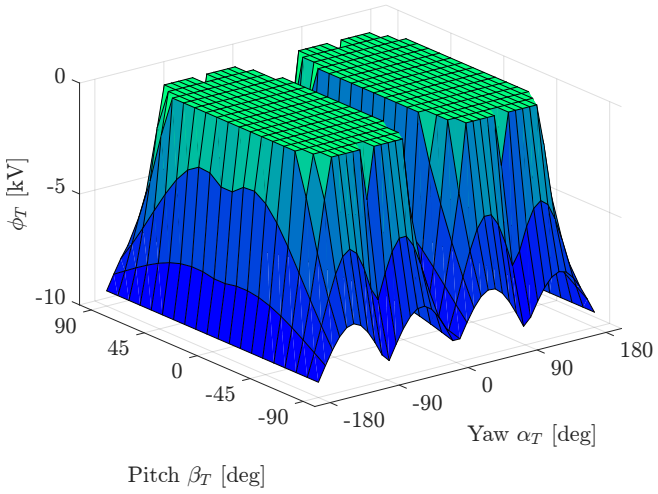

Figure 6. Electric Potential of the target ϕ_T as function of target orientation

and $T_i = 8,000$ eV. An electron beam is included with an energy of $E_{EB} = 30$ keV and a current of $I_{EB} = 2$ mA. The spacecraft centers are 15 m apart, with their nominal orientation shown in Fig. 3, and the sun direction is aligned with the nominal $\hat{\boldsymbol{t}}_1$ direction.

Figure 6 shows the equilibrium potential of the GOES-R target satellite as a function of its orientation. The orientation of the target is changed using yaw and pitch 3-2-1 Euler rotations as depicted in Fig. 3, while the servicer remains at the nominal orientation. For orientations where the yaw angle is close to $\alpha_T = \{-180°, 0°, 180°\}$ or the pitch angle is close to $\beta_T = \{-90°, 90°\}$, the equilibrium potential is highly negative, while it is approximately zero for all other orientations. The aforementioned angles correspond to those orientations where the solar panel of the GOES-R satellite is edge on with the sun, that is, the normal vectors of the two panel facets are (nearly) perpendicular to the sun direction $\hat{\boldsymbol{s}}$. If the solar panel normal vector is more aligned with the sun direction, the sunlit area is increased, providing a greater photoelectric current. Because the released photoelectrons are attracted back to the spacecraft once it is positively charged, the target settles to an equilibrium potential that is only a few volts positive (close to zero). The equilibrium potential of the servicer is about $+15$ kV due to the electron beam current. It should be noted that a roll rotation about the $\hat{\boldsymbol{t}}_2$ axis also affects the resulting potential, force and torque. It is neglected here because the important orientations such as the solar panel facing (or not facing) the Sun as well as the solar panel pointing at the servicer (or not) are also covered using only yaw and pitch.

To study the effect of the orientation-dependent equilibrium potential on electrostatic proximity operations, four different models are considered to compute the electrostatic force and torque as a function of the target orientation. The highest-fidelity model uses the faceted model to compute the electric potential of the spacecraft and the multi-sphere model (MSM) to calculate the resulting force and torque (Model 1 – "faceted, MSM"), while the lowest-fidelity model uses a spherical spacecraft to determine the potential and a 1-sphere model (1SM) to approximate the force and torque (Model 4 – "spherical, 1SM"). Two more models are studied that are a mix of the highest and lowest fidelity models (Model 2 – "spherical, MSM" and Model 3 – "faceted, 1SM"). The radius R_{eff} of the single sphere is chosen to match the self-capacitance C of the MSM model

$$R_{\text{eff}} = \frac{C}{4\pi\epsilon_0} \tag{28}$$

where ϵ_0 is the vacuum permittivity. This radius is referred to as the effective radius, and is equal to 4.4438 m for the GOES-R and 4.7984 m for the SSL-1300 satellite. Essentially, the faceted model accounts for the effect of the orientation on the equilibrium potential (which affects the force and torque), while the Multi-Sphere model accounts for the direct effect of the orientation on the electrostatic force and torque.

Figure 7 shows the electrostatic force between the servicer and target as a function of the target orientation for the different models. There are three clear peaks in force magnitude for the highest-fidelity model. These peaks also exist for the "spherical, MSM" model and are a consequence of the solar panel of the target pointing towards the servicer. However, this effect is pronounced for the highest-fidelity model, because the solar panel is edge on with the sun for these orientations, leading to a more negative electric potential that further increases the electrostatic force. The force magnitude for the "faceted, 1SM" model essentially corresponds to Fig. 6, but flipped upside down. When the electric potential is more negative, the force is greater due to the positively charged servicing spacecraft. Finally, the force for the "spherical, 1SM" model is constant across all orientations.

The electrostatic torque as a function of yaw and pitch angles is shown in Fig. 8. For the 1-sphere models (Model 3 and 4), the torque is zero across all orientations, because the center of charge is always aligned with the center of mass for a single sphere, producing no torque. The observations for the torque of the MSM models (Models 1 and 2) are similar to the observations above for the force magnitude. Model 2 accounts for the torque variations due to different orientations, but, for the given GOES-R spacecraft model, these variations are enhanced by the orientation-dependent equilibrium potential.

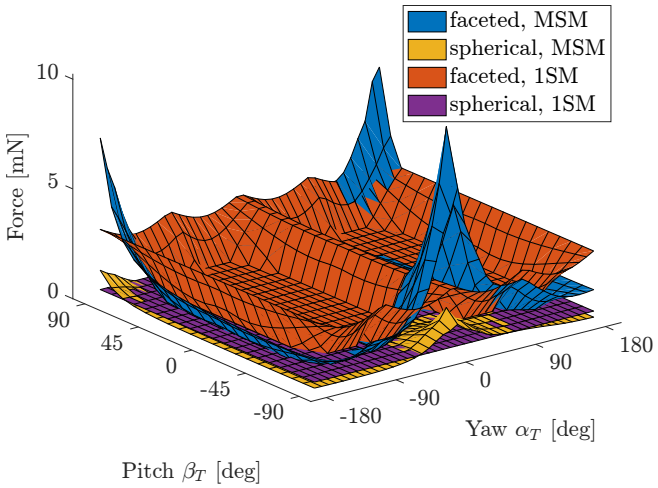

Figure 7. Electrostatic force magnitude as function of target orientation, using different models

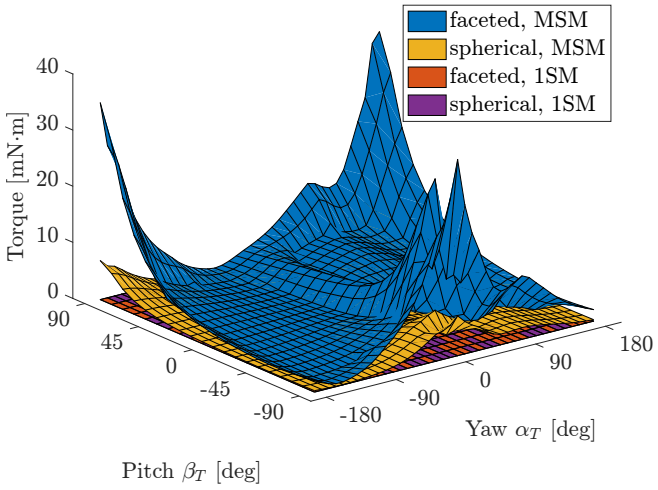

Figure 8. Electrostatic torque magnitude as function of target orientation, using different models

A dynamic simulation is performed, where the relative position of the two spacecraft and the attitude of the servicer are held constant, but the target satellite is free to rotate given the electrostatic torque that is acting on it (Fig. 9). The initial attitude corresponds to the nominal orientation shown in Fig. 3, with zero angular velocity. Due to the electrostatic torque, the target starts rotating. Because the 1-sphere model cannot account for any torques, the orientation of the target stays constant throughout the simulation and neither the potential nor the force change. In case of the "faceted, 1SM" model, the potential remains at about -10 kV, because the sunlit area of the faceted model at its initial (and in this case constant) orientation is rather small, causing a strong force, but no torque.

The cases of the multi-sphere models are more interesting. Due to the large cross-section of the 4.4438 m radius GOES-R effective sphere that is facing the Sun, the equilibrium potential is about 0 V for the "spherical, MSM" model, at all times. Regardless of the 0 V potential, the electrostatic

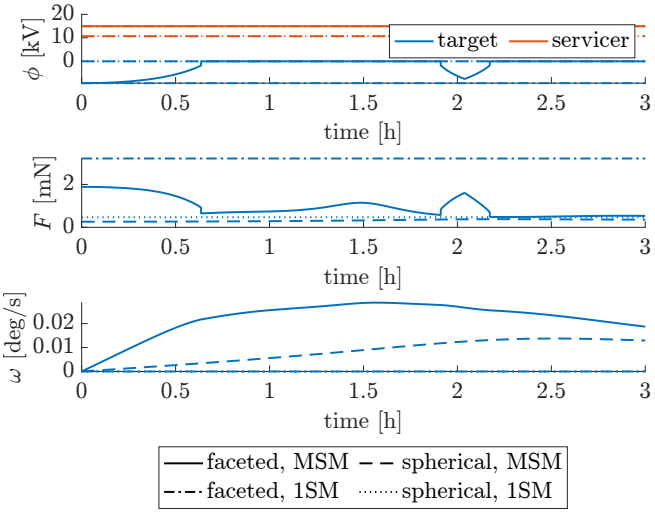

Figure 9. Electric potential ϕ of target and servicer, force magnitude F and rotational rate ω over time

force and torque are non-zero due to induced charging effects [23]. The force and torque are rather small in magnitude, so the rotational rate of the target is small as well. Finally, the "faceted, MSM" model provides the most interesting case. Initially, the potential of the target spacecraft is at about -10 kV. As the target starts rotating due to the electrostatic torque, the sunlit area increases, which makes the equilibrium potential less negative. At some point, the potential is close to zero and the force is significantly lower than at the beginning. After about 2 hours, only a small area of the target spacecraft is in sunlight once again, causing a spike in the equilibrium potential and the electrostatic force. The rotational rate of the target is higher for Model 1 compared to Model 2, due to the generally higher electrostatic force and torque for Model 1. The differences between these models depend on the specific shapes of the spacecraft, but the results demonstrate that the charge distribution and dynamics can be misrepresented by a spherical, 1-sphere model.

5. Adjusted Sphere Model

The equations for the plasma currents provided in Eqs. (3) and (4) can be adjusted using the parameters μ and α [24]

$$I_e(\phi) = \begin{cases} -\frac{Aq_0 n_e w_e}{4} \mu e^{\phi/T_e} & \text{if} \quad \phi \leq 0 \\ -\frac{Aq_0 n_e w_e}{4} \mu \left(1 + \frac{\phi}{T_e}\right)^{\alpha} & \text{if} \quad \phi > 0 \end{cases} \tag{29}$$

$$I_i(\phi) = \begin{cases} \frac{Aq_0 n_i w_i}{4} \mu \left(1 - \frac{\phi}{T_i}\right)^{\alpha} & \text{if} \quad \phi \leq 0 \\ \frac{Aq_0 n_i w_i}{4} \mu e^{-\phi/T_i} & \text{if} \quad \phi > 0 \end{cases} \tag{30}$$

The parameters μ and α are determined by fitting these functions to charging data obtained from Nascap, for example, or in-orbit measurements, if available. A charging simulation is performed with Nascap for the GEO worst-case scenario and the GOES-R shape, and the ion current is saved as a function of the spacecraft potential. Matlab's `lsqnonlin()` function is used to fit the parameters to the charging data recorded in Nascap, using the surface area A that corresponds to the effective GOES-R sphere model. The nonlinear least

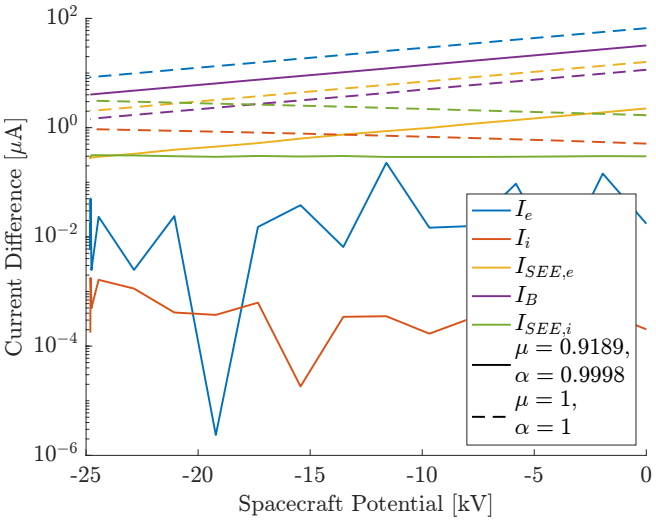

Figure 10. Adjusted Sphere Model

squares fit yields $\mu = 0.9189$ and $\alpha = 0.9998$. Figure 10 shows the difference between the currents computed with the adjusted sphere model and the currents obtained in Nascap. Essentially, for this rather simple charging environment that assumes a Maxwellian plasma, the parameter α stays very close to 1, while the factor μ scales the surface area of the sphere to match the surface area of the actual GOES-R spacecraft. Thus, the current differences in Fig. 10 for $\mu = 0.9189$ and $\alpha = 0.9998$ are the same as the differences observed for the GOES-R shape in Fig. 5. The same random behavior of the plasma currents is visible due to the precision of 4 significant digits that is used to compute the currents in Nascap-2k.

Conclusions

This work compares several reduced-order spacecraft charging models with the motivation of accurately computing the electrostatic force and torque acting on two spacecraft during proximity operations. The simplest model uses a simple sphere with an effective radius based on the self-capacitance of the spacecraft to compute the resulting environmental currents. Another model is also based on a sphere, but uses adjusted charging equations that introduce two parameters. These parameters are fitted by nonlinear least squares to charging data generated with higher-order spacecraft charging software such as Nascap-2k and SPIS, or to real-world charging data obtained from in-orbit measurements. The last model divides the spacecraft surface into several facets. Not only does this approximate the total surface area of the spacecraft more accurately, but it also allows for the consideration of a time-varying sunlit area, which affects the photoelectric current.

While the effective radius based on the self-capacitance of a spacecraft is convenient for studying charging transients, the resulting surface area might not be very accurate. This can lead to large errors in the computed environmental plasma and secondary currents. By using an adjusted sphere model, the total surface area is essentially scaled by the first parameter μ to match the area of the actual spacecraft, which improves the accuracy of the model. For the simple charging environment studied in this work, no significant adjustments were required for the second parameter α, but this is likely not the case for more complex environments such as the auroral regions. Finally, the faceted model allows for the orientation-dependent computation of the electric potential due to a better approximation of the sunlit area. A dynamic simulation shows that, for the spacecraft shapes used in this work, the equilibrium potential and the resulting electrostatic force and torque can significantly vary between a faceted and a spherical model.

Acknowledgments

This work was supported by the U.S. Air Force Office of Scientific Research under grant FA9550-20-1-0025. Julian Hammerl gratefully acknowledges funding from the NASA FINESST fellowship (award number 80NSSC22K1849), and Kaylee Champion thanks the NASA NSTGRO fellowship.

References

[1] S. T. Lai, *Fundamentals of Spacecraft Charging*. Princeton University Press, Oct. 2011.

[2] R. C. Olsen, "Record charging events from Applied Technology Satellite 6," *Journal of Spacecraft and Rockets*, vol. 24, no. 4, pp. 362–366, Jul. 1987.

[3] H. B. Garrett and A. C. Whittlesey, *Guide to Mitigating Spacecraft Charging Effects*. Hoboken, NJ, USA: John Wiley & Sons, Inc., May 2012.

[4] I. Katz, V. Davis, and D. Snyder, "Mechanism for spacecraft charging initiated destruction of solar arrays in GEO," in *36th AIAA Aerospace Sciences Meeting and Exhibit*. AIAA Paper 1998-1002, Jan. 1998, pp. 1–5.

[5] H. Brandhorst and J. Rodiek, "Improving Space Utilization by Increasing Solar Array Reliability," in *AIAA SPACE 2007 Conference and Exposition*. AIAA Paper 2007-6024, Sep. 2007, pp. 1–5.

[6] K. Wilson and H. Schaub, "Impact of Electrostatic Perturbations on Proximity Operations in High Earth Orbits," *Journal of Spacecraft and Rockets*, vol. 58, no. 5, pp. 1293–1302, 2021.

[7] H. Schaub and D. F. Moorer, "Geosynchronous Large Debris Reorbiter: Challenges and Prospects," *The Journal of the Astronautical Sciences*, vol. 59, no. 1-2, pp. 161–176, Jun. 2012.

[8] H. Schaub and D. Stevenson, "Prospects of Relative Attitude Control Using Coulomb Actuation," *The Journal of the Astronautical Sciences*, vol. 60, no. 3-4, pp. 258–277, Dec. 2013.

[9] K. Wilson, Á. Romero-Calvo, and H. Schaub, "Constrained Guidance for Spacecraft Proximity Operations Under Electrostatic Perturbations," *Journal of Spacecraft and Rockets*, vol. 59, no. 4, pp. 1304–1316, 2022.

[10] H. Schaub and Z. Sternovsky, "Active space debris charging for contactless electrostatic disposal maneuvers," *Advances in Space Research*, vol. 53, no. 1, pp. 110–118, Jan. 2014.

[11] J. A. Hughes and H. Schaub, "Electrostatic Tractor Analysis Using a Measured Flux Model," *Journal of Spacecraft and Rockets*, vol. 57, no. 2, pp. 207–216, Mar. 2020.

[12] J. Hammerl and H. Schaub, "Debris Attitude Effects on Electrostatic Tractor Relative Motion Control Performance," in *Proceedings of the AAS/AIAA Astrodynamics Specialist Conference*. AAS Paper 21-548, Aug. 2021, pp. 1–13.

[13] D. Stevenson and H. Schaub, "Multi-Sphere Method for modeling spacecraft electrostatic forces and torques," *Advances in Space Research*, vol. 51, no. 1, pp. 10–20, Jan. 2013.

[14] V. A. Davis and M. J. Mandell, "NASCAP-2K Version 4.3 Scientific Documentation," Air Force Research Laboratory, Tech. Rep., 2016.

[15] V. A. Davis, M. J. Mandell, and M. F. Thomsen, "Representation of the measured geosynchronous plasma environment in spacecraft charging calculations," *Journal of Geophysical Research: Space Physics*, vol. 113, no. A10, pp. 1–14, Oct. 2008.

[16] R. Hippler, S. Pfau, M. Schmidt, and K. H. Schoenbach, *Low Temperature Plasma Physics: Fundamental Aspects and Applications*, 1st ed. Wiley, 2001.

[17] Á. Romero-Calvo, G. Cano-Gómez, and H. Schaub, "Simulation and Uncertainty Quantification of Electron Beams in Active Spacecraft Charging Scenarios," *Journal of Spacecraft and Rockets*, vol. 59, no. 3, pp. 739–750, May 2022.

[18] J. A. Hughes and H. Schaub, "Heterogeneous Surface Multisphere Models Using Method of Moments Foundations," *Journal of Spacecraft and Rockets*, vol. 56, no. 4, pp. 1259–1266, Jul. 2019.

[19] J. Hammerl and H. Schaub, "Effects of Electric Potential Uncertainty on Electrostatic Tractor Relative Motion Control Equilibria," *Journal of Spacecraft and Rockets*, vol. 59, no. 2, pp. 552–562, Mar. 2022.

[20] H. Schaub and J. L. Junkins, *Analytical Mechanics of Space Systems*, 4th ed. Reston, VA: AIAA Education Series, 2018.

[21] K. T. H. Wilson, "Remote Electrostatic Potential Determination for Spacecraft Relative Motion Control," Doctoral Thesis, University of Colorado Boulder, 2021.

[22] M. H. Denton, "Bulk plasma properties at geosynchronous orbit," *Journal of Geophysical Research*, vol. 110, no. A7, p. A07223, 2005.

[23] H. Schaub and L. E. Jasper, "Orbit boosting maneuvers for two-craft coulomb formations," *Journal of Guidance, Control, and Dynamics*, vol. 36, no. 1, pp. 74–82, 2013.

[24] S. T. Lai, "An improved Langmuir probe formula for modeling satellite interactions with near-geostationary environment," *Journal of Geophysical Research*, vol. 99, no. A1, p. 459, 1994.

BIOGRAPHY

Julian Hammerl *is a Ph.D. student in the Autonomous Vehicle Systems (AVS) Laboratory of the Aerospace Engineering Sciences department at the University of Colorado Boulder. He received his Bachelor's degree in Mechanical Engineering in 2020 from the Vienna University of Technology in Austria. Julian received the NASA FINESST fellowship in 2022. His research interests include spacecraft guidance and control, charged astrodynamics, active space debris removal, and remote sensing of electric potentials.*

Kaylee Champion *received a B.S. degree in aerospace engineering from the University of Texas, Austin, TX, USA, in 2021 and is currently pursuing a PhD degree in astrodynamics at the University of Colorado Boulder, Boulder, CO, USA. She received the National Science Foundation fellowship in 2021 and the NSTGRO fellowship in 2022. Her current research interests include charged astrodynamics, spacecraft-plasma interactions, and mitigating space debris.*

Hanspeter Schaub *is a professor and chair of the University of Colorado aerospace engineering sciences department. He holds the Schaden leadership chair. He has over 28 years of research experience, of which 4 years are at Sandia National Laboratories. His research interests are in astrodynamics, relative motion dynamics, charged spacecraft motion as well as spacecraft autonomy. This has led to about 207 journal and 327 conference publications, as well as a 4th edition textbook on analytical mechanics of space systems. Dr. Schaub has been the ADCS lead in the CICERO mission, the ADCS algorithm lead on a Mars mission and supporting ADCS for a new asteroid mission. He has been awarded the H. Joseph Smead Faculty Fellowship, the Provost's Faculty Achievement Award, the faculty assembly award for excellence in teaching, as well as the Outstanding Faculty Advisor Award. He is a fellow of AIAA and AAS, and has won the AIAA/ASEE Atwood Educator award, AIAA Mechanics and Control of Flight award, as well as the Collegiate Educator of the Year for the AIAA Rocky Mountain section.*